

Large-volume and shallow magma intrusions in the Blackfoot Reservoir volcanic field (Idaho, USA)

M. S. Hastings¹, C. B. Connor¹, P. Wetmore¹, R. Malservisi¹, L. J. Connor¹,
M. Rodgers¹, P. C. La Femina²

¹School of Geosciences, University of South Florida

²Department of Geosciences, The Pennsylvania State University

Key Points:

- Large-amplitude gravity anomalies are mapped in a combined terrestrial and marine gravity survey in the Blackfoot Reservoir volcanic field, Idaho (BRVF), adjacent to young (1.5 Ma, 58 ka) topaz rhyolite domes and tuff rings within a Quaternary basaltic volcanic field.
- Best-fit 3D inversion of the gravity data, constrained by density contrast estimates and excess mass calculations, indicates the presence of two intrusions of laccolithic shape in the uppermost crust, with cumulative volume of $\sim 63 \text{ km}^3$ and volume uncertainty in the range $50 - 120 \text{ km}^3$.
- Extensive volcanotectonic interaction during emplacement is identified by comparing mapped gravity with fault distribution and throw. The western edges of the gravity anomalies coincide with normal faults with vertical displacements that range from $5 - 10 \text{ m}$ (maximum 50 m).
- The potential exists for future large-volume silicic eruptions in the BRVF and similar bimodal volcanic fields, such as those found in the western U.S.

Corresponding author: M. S. Hastings, mshastings1@usf.edu

Abstract

The Blackfoot Reservoir volcanic field (BRVF), Idaho, USA, is a bimodal volcanic field that has hosted explosive silicic eruptions during at least two episodes, as recently as 58 ka. Using newly collected terrestrial and marine gravity data, two large negative anomalies (-16 mGal) are modeled as shallow (< 1 km) laccoliths beneath a NE-trending alignment of BRVF rhyolite domes and tuff rings. Given the trade-off between density contrast and model volume, best-fit gravity inversion models yield a total intrusion volume of $50\text{--}120$ km³; a density contrast of -600 kg m⁻³ results in model intrusion volume of 63 km³. A distinctive network of $340^\circ\text{--}360^\circ$ trending faults lies directly above and on the margins of the mapped gravity anomalies. Most of these faults have $5\text{--}10$ m throw; one has throw up to ~ 50 m. We suggest that the emplacement of shallow laccoliths produced this fault zone and also created a ENE-trending fault set, indicating widespread ground deformation during intrusion emplacement. The intrusions and silicic domes are located $3\text{--}5$ km E of a regional, 20 mGal step in gravity. We interpret this step in gravity as a change in the thickness of the Upper Precambrian to lowermost Cambrian quartzites in the Meade thrust sheet, part of the Idaho-Wyoming Thrust Belt. Silicic volcanism in the BRVF is a classic example of volcanotectonic interaction, influenced by regional structure and creating widespread deformation. Exogenous and endogenous domes are numerous in the region. We suggest volcanic hazard assessments should account for potentially large-volume silicic eruptions in the future.

Plain Language Summary

On Earth, gravity anomalies occur where there are significant, subsurface, lateral density variations. We map two gravity anomalies located in the Blackfoot Reservoir volcanic field, Idaho, a site which has experienced explosive volcanic eruptions as recently as 58,000 years ago. Our numerical models of the gravity anomalies indicate that they are caused by two saucer-shaped intrusions, magma bodies that likely fed eruptions at the surface and triggered fault displacement. Although these magma bodies have cooled, they have large volumes and suggest that large-volume explosive volcanic eruptions are possible in this volcanic field in the future.

1 Introduction

Bimodal volcanic fields comprise multiple vents that have erupted basalt and dacite to rhyolite with no intermediate compositions (Bacon, 1982; Suneson, 1983; Tanaka et al., 1986). Silicic eruptions in bimodal volcanic fields have potentially unexpected impacts as these eruptions are not associated with long-lived or frequently active volcanic systems. Yet, these eruptions tend to be more intense, voluminous and of longer duration than basaltic counterparts (Sparks, 2003; Connor et al., 2009). Like silicic eruptions at composite volcanoes and calderas, formation of a new silicic vent in a distributed volcanic field can produce tephra fallout, block and ash flows, surges and long-active domes (Pardo et al., 2009; Avellán et al., 2012; McCurry & Welhan, 2012; Gómez-Vasconcelos et al., 2020). The dynamics of magma intrusion and the eruption of new silicic vents are both influenced by tectonic setting and local structures. These events cause surface deformation that extends hundreds to thousands of meters beyond the vent area (Mastin & Pollard, 1988; Jay et al., 2014; Castro et al., 2016). By studying the silicic intrusions that feed these eruptions, we can better understand precursors to new eruptions in bimodal volcanic fields and better anticipate their potential impacts.

The Blackfoot Reservoir volcanic field (BRVF), located in the northeast Basin and Range of the western USA (Figure 1), is a bimodal volcanic field (McCurry & Welhan, 2012). We use new terrestrial and marine gravity data collected to constrain the volumes and geometries of two shallow intrusions associated with an alignment of five silicic domes

and explosion craters, erupted approximately 58 ka, in an area called the Central Dome Field (CDF) located within the BRVF (Figure 2a). The edges of the modeled intrusions are marked by a network of N to NNW-trending surface faults that are unique to the region in their variable along-strike displacement and *en echelon*, corrugated map pattern (Polun, 2011; McCurry & Welhan, 2012). These features suggest that these are young normal faults (Ferrill et al., 1999), similar to those produced by volcanotectonic interaction mapped in other volcanic fields (Bacon et al., 1980; Bursik & Sieh, 1989; Mazzarini et al., 2004; Tuffen & Dingwell, 2005; Gottsmann et al., 2009; Garibaldi et al., 2020). The intrusions are directly overlain by a second fault set. These ENE-trending surface faults have smaller displacements (Figures 2b and 3).

We present 3D gravity models of shallow intrusions in the CDF. The models are calibrated with the density of nearby silicic domes and with an excess mass calculation. We estimate the volumes of the intrusions and the domes to constrain the intrusive to extrusive volume ratio. The locations and displacements of faults (Polun, 2011; McCurry & Welhan, 2012) are found to coincide with the modeled intrusions. (Figures 2a and b, Figure 3). Our results suggest that potential future silicic eruptions may have large volumes and could be accompanied by widespread surface deformation. Results also suggest that regional tectonic structures may influence magma ascent and accumulation in the shallow crust, as found in other volcanic systems (Bacon et al., 1980; Acocella & Funicello, 1999; White et al., 2015; Deng et al., 2017).

2 Overview of BRVF geology

The BRVF lies in the transition between the Intermontane Seismic Belt and a seismically quiescent region that includes the Eastern Snake River Plain (ESRP) (Anders et al., 1989). This distributed volcanic field comprises Quaternary scoria cones, basalt flows, rhyolitic domes, and tuff rings (Figure 3). There are three rhyolitic domes at the southern end of the Blackfoot Reservoir, named China Hat¹, China Cap², and North Cone. These three domes and nearby tuff rings make up a NE-trending volcano vent alignment that defines the CDF (Figure 2b). The base of the China Hat and China Cap domes are primarily block and ash flows with surge deposits exposed in a quarry at the base of China Hat dome. The craters of two tuff rings, Burchett Lake and Gronewell Lake, are filled with water. These tuff rings have low outer slopes typical of surge deposits associated with phreatomagmatic eruptions (Figure 2b). The China Cap dome has been dated using ⁴⁰Ar/³⁹Ar, yielding an age of 58 ka (Heumann, 2004).

The basaltic lavas of the BRVF erupted from low scoria cones and fissures. Basalt lava flows reach a thickness of 290 m in the CDF, where they surround the silicic vents and cap the underlying geology as a continuous lava flow field. Basalt eruptions in the BRVF have poor age constraints. Some of the lavas from the BRVF flowed out to the southwest into Gem Valley (Figure 1). These have been dated radiometrically between 100 and 25 ka (McCurry et al., 2011). Basalt vent alignments also occur in Gem Valley.

Mapping of the surrounding bedrock geology reveals several generations of faults including NW-trending, SW-dipping thrust faults of the Idaho-Wyoming Thrust Belt (Figures 2 and 3) formed during the Jura-Cretaceous Sevier Orogeny (Armstrong & Oriel, 1965; Dixon, 1982). NW-trending normal faults, perhaps representing two phases of late Tertiary extension, overprint these older faults. In addition to these older structures, there is a third set of distinctive normal faults (Polun, 2011) (Figures 2 and 3) that are only

¹ Alternative, or appropriate, names unfortunately do not exist. As such, we use the names present in the literature

² See footnote 1

found within the BRVF. We evaluate the origin of these latter faults and their relationships to silicic volcanic vents in light of gravity anomalies and models, described below.

3 Gravity data collection and processing

Mabey & Oriel (1970) first identified negative gravity anomalies in the CDF, which they interpreted as shallow sedimentary basins. We provide evidence that these negative gravity anomalies are instead caused by shallow intrusive rocks, given the spatial association of these anomalies with young silicic domes of the CDF and nearby faults. Prominent gravity anomalies are associated with silicic intrusions elsewhere (Bott & Smithson, 1967; Finn & Williams, 1982; Blakely, 1994; Battaglia et al., 2003; George et al., 2016; Miller et al., 2017; Paulatto et al., 2019).

New gravity data were collected broadly throughout the BRVF, with higher density sampling in and around the CDF. These data were merged with the regional database (Keller et al., 2006), consisting almost entirely of data collected by the USGS, including survey data collected by Mabey & Oriel (1970). In addition to terrestrial data, we collected marine gravity data over the reservoir to better constrain the lateral extent of the large negative anomalies and steep gravity gradients (Figures 4 and 5a).

A total of 460 new terrestrial gravity measurements were made with a Burris gravimeter (B-38) with measurement precision of approximately 0.003 mGal. Station location was determined using a Trimble R10 and CenterPoint RTX service, which has a horizontal precision of 3–5 cm and a vertical precision of 7–10 cm (Glocker et al., 2012). After correcting for an instrument drift of ± 0.025 mGal/day, the uncertainty on our gravity measurements is ± 0.03 mGal.

Terrestrial gravity data reduction included tidal, latitude, atmospheric mass, free-air, spherical cap Bouguer and terrain corrections (White et al., 2015). These corrections were applied to the new data and to the drift-corrected regional data from the USGS to achieve consistency among gravity data from different sources. The terrain correction was applied in two parts, an inner correction using a 10 m DEM with 20 km radius about each gravity station, and an outer correction using a 30 m DEM with 167 km radius about each station. The DEM data used for the terrain corrections were obtained from the USGS National Elevation Database (NED), and a density of 2670 kg m^{-3} was used for Bouguer and terrain corrections (Hinze, 2003). Gravity was remeasured at several USGS gravity station locations to use as tie-in points, similar to the procedure in Deng et al. (2017).

The terrestrial gravity data reveal a large amplitude (~ 21 mGal) negative anomaly in the CDF with a gravity gradient under the reservoir (Figure 4). We collected over 14,000 data points with a Dynamic Gravity Systems (DGS) Marine Gravity Sensor (AT1M) on a pontoon boat to define the shape and gradient of the gravity anomaly in the reservoir. (Figure 5a). This gravimeter is gimbaled to compensate for the accelerations imposed by the motion of the boat. The same corrections made to the terrestrial data were applied to the marine data, with additional corrections accounting for the motion of the gravimeter. The Eötvös correction was applied to account for the velocity of the boat as it adds or subtracts to the tangential velocity of the gravimeter relative to the rotational axis of Earth, and the acceleration of the platform the gravimeter rests on was accounted for in the inertial reference frame of the vessel (Telford et al., 1990). A correction was made for the mass of water in the reservoir, although this is found to have trivial impact as the reservoir is < 10 m deep and changes depth very gradually (Wood et al., 2011). The velocity and acceleration of the vessel were obtained through the differentiation and double differentiation of the GPS position, respectively.

The marine data were sampled at a rate of 1 Hz on a continuously moving platform, leading to a higher spatial density of measurements on the reservoir compared to the terrestrial measurements. Including all of the marine data in our gravity model would cause

the region beneath the reservoir to be over-constrained leaving the more sparsely sampled terrestrial regions to be comparatively under-constrained and less significant in the gravity model. Consequently, the marine data were sampled every 100 meters along the survey track lines to mitigate over-constraining the region beneath the Blackfoot Reservoir during the inversion.

The combined terrestrial and marine data were further filtered to include only a 780 km² area (3126 measurements), centered on the two negative CDF gravity anomalies (Figure 5a and b). This filtering helps to identify longer wavelength, regional signals that underlie the negative anomalies in the BRVF and to separate these shorter wavelength gravity anomalies from the regional gravity, as described in the next section. Both the entire data set and the grid of sub-sampled data used to model the anomalies are provided in the supplementary material.

4 Isolation of the CDF gravity anomalies

Gravity anomalies arise from a combination of broader regional effects of the basement structure and shorter wavelength anomalies produced by local mass variations in the shallower subsurface. Separating the local gravity anomalies from the regional gravity signal is paramount to interpreting and modeling the gravity data. The complete Bouguer gravity map of the CDF (Figure 5b) includes two distinct, negative gravity anomalies with magnitude of approximately -21 mGal. These short wavelength anomalies lie within a regional gravity anomaly, with high amplitude positive values (20 mGal) to the west and low amplitude negative (-5 mGal) values to the east (Figure 4). The regional variation does not correlate with the topography, and the transition between the positive and negative values happens over a relatively short distance (~ 8 km). This gradient is not linear, but shows a step in the regional gravity that is located 2 – 3 km west of the rhyolite domes in the CDF (Figure 5b).

To isolate the regional gravity trend, data that are more negative than a -6 mGal threshold are removed (Figure 5c). The filtered data that were removed are the local gravity anomalies. The threshold value used to separate the regional anomaly from the local is subtracted from the local data and these data are contoured (Figure 5d). The filtered local gravity anomaly has an amplitude of approximately -15 mGal, with clear separation from other sources of anomalous gravity. Adding the two maps (Figures 5c and d) gives the original gravity map (Figure 5b).

The regional, long-wavelength gravity anomaly (Figure 5c) shows a large amplitude positive anomaly (20 mGal) over the range between Gem Valley and the BRVF. A cross-sectional profile from Dixon (1982) (his number 17) depicts the west-dipping Meade thrust fault cutting and displacing the contact between the Precambrian and Cambrian (1–3 km depth). This displacement shallows and thickens quartzites beneath the range on the western edge of the BRVF. We suggest that the observed regional gravity step correlates to the approximate eastern limit of the quartzites that are displaced in the Meade thrust fault.

The local gravity anomalies have elliptical shapes, each striking NW–SE. The two negative anomalies are separated by a saddle of higher gravity values (Figure 5d). The domes and tuff rings lie within and near this saddle. The volcano vent alignment is nearly orthogonal in trend to the long-axes of the negative anomalies. The faults in the BRVF appear to wrap around the negative anomalies on the west side of China Hat dome and the western margin of Blackfoot Reservoir (Figure 5d).

5 Constraints on the gravity model

The two negative CDF gravity anomalies (Figure 5d) represent a mass deficit. We calculate the mass deficit, ΔM , using Green's function (Parker, 1974):

$$\Delta M = \frac{1}{2\pi G} \sum_{i=1}^N \sum_{j=1}^M \Delta g(x, y) \Delta x \Delta y$$

where $\Delta g(x, y)$ is the gravity anomaly, N and M are the number of grid points in the X (easting) and Y (northing) directions, respectively, and Δx and Δy is the grid spacing (500 m) in the X and Y directions. This integration of the detrended gravity data gives a mass deficit of -3.5×10^{13} kg. For a reasonable range of density contrasts, the mass deficit calculation shows that the causative body of these anomalies is of order tens of cubic kilometers of material.

Hand samples of rhyolite from the China Cap dome yield unsaturated bulk rock densities of $1600 - 1800 \text{ kg m}^{-3}$. The Nettleton and Parasnis approaches to modeling bulk density from gravity profile data (Nettleton, 1939; Parasnis, 1952; Agustsdottir et al., 2011; Saballos et al., 2013) yield a bulk dome density of about 1700 kg m^{-3} for China Cap dome, which is consistent with bulk silicic dome densities determined using the same methods elsewhere (Agustsdottir et al., 2011). We assume that the density contrast between intrusive silicic rocks and the crust is not as large as the density contrast between the rhyolite dome and the crust, but it may approach this value. Additionally, density estimates of A-type granophyres and rhyolite intrusions are as high as 2400 kg m^{-3} (Lowenstern et al., 1997).

The Hubbard 25-1 Borehole (Figure 2b), drilled in 1983, provides constraints on the density and lithology of the country rock within the upper crust of the BRVF (Polun, 2011). The well is located approximately 1.5 km south of China Hat and approximately 1 km west of the edge of the southern negative gravity anomaly (Figure 5b). The compensated neutron lithodensity logs contain data that constrains the bulk density as a function of depth within the borehole. The range of densities within the log spans from $2600 - 2800 \text{ kg m}^{-3}$ with an average density over the entire 2 km section of 2700 kg m^{-3} (Figure 6). The lithology within this well alternates between basalts, siltstones, and shales near the surface to interbedded limestones, sandstones, and shales at depth. The thickness of basalts in the uppermost part of the log is approximately 290 m including scoria layers, constraining the thickness of BRVF basalts. We were unable to determine from the logs if the deeper basalts (750 m and 1100 m) are extrusive or intrusive. Nevertheless, we are confident that igneous rocks are present at these depth intervals.

Given a mass deficit of -3.5×10^{13} kg, for density contrasts -800 to -400 kg m^{-3} , the causative body has a volume range of $44 - 88 \text{ km}^3$. This range of density contrasts is used in our gravity inversion models and our model results are compared with this range of volume estimates.

6 Gravity modeling of regional and local anomalies

Inverse modeling is used to deduce subsurface structure both for regional and local anomalies (Figures 5c and d). Our modeling approach first discretizes the subsurface into a grid of vertical-sided rectangular prisms (i.e., the blue grids in Figures 5c and d). We assume a constant density contrast between all prisms and the surrounding bedrock, but the magnitude of this density contrast is solved during inverse modeling of the gravity data.

6.1 Inversion procedure

Two inversion procedures are used, one to model the regional signal and one for the local anomalies. Regional inversion modeling assumes a single bottom depth for all prisms, while local inversion modeling uses unique top and bottom depths for each prism. Inputs to the inversion include a range for each adjustable parameter value (*depth-to-bottom*, *depth-to-top*, *density contrast*). Both inversions initialize multiple sets of initial parameter guesses, drawn from input ranges specified in a configuration file. The total number of parameter sets is one more than the total number of modifiable parameters. The local inversion model has 391 independent model parameters, resulting in the initialization of 392 unique sets of randomized parameters; the regional inversion model has 58 independent model parameters, resulting in the initialization of 59 unique sets of randomized parameters.

The inversion process adjusts and tests these parameter combinations, using a calculated solution for the gravity due to a prism. The *gbox* solution for gravity (Blakely, 1996), written in C for speed, is used as the forward model. The gravity anomaly associated with each prism is summed across the map area and then compared with observed gravity values interpolated on to a grid. Interpolated and gridded gravity values are used because of variability in the density of gravity measurements across the region and to speed calculations. The grid size for the inversion process is selected by experimentation to minimize the number of model parameters and to best resolve the subsurface structure. Modeling a large number of small prisms often results in an awkward prism solution that requires additional smoothing, which does not necessarily improve the model (White et al., 2015). Our modeling attempts using a large number of small prisms created unrealistic bumps and rapid changes in prism thickness, resulting in an unrealistic model geometry given the relatively smooth variation in the observed gravity.

The downhill-simplex optimization algorithm (Nelder & Mead, 1965; Press et al., 2007) is used to resolve and identify a best set of model parameters based on a goodness-of-fit test designed to minimize the residual error between the measured data and the calculated solution. We use the root-mean-squared error (RMSE) for this goodness-of-fit test. Typically, 100,000 – 200,000 forward solutions are calculated to find a best-fit model. Multiple simulations are completed by varying the random seed and prism boundaries to fully explore the model parameter space and to identify local minima.

6.2 Regional model

The model of the regional gravity field (Figure 5c) is based on the interpretation that a thickening of Precambrian quartzites in the Meade thrust fault exists near the western edge of the BRVF (Dixon, 1982). The prism size used for the regional model is 4×4 km, due to the more widely-spaced gravity data to the west of the BRVF. We model the regional data with a flat-bottomed geometry to more closely emulate the thickening of quartzites on the west side of the BRVF. The modeled density contrast ranges from 0 to 150 kg m⁻³ and the modeled depth range for the quartzite contact is 0.5–12 km. The model prisms extend slightly beyond the data boundaries to resolve edge effects and better constrain the gravity anomalies at the edges of the model area (Figure 5c).

Figure 7 shows the geometry of the best-fit inversion model for the regional gravity data. The depth-to-bottom is 8.1 km; all models solved for a density contrast around 150 kg m⁻³. The average depth-to-top on the western margin of the region is ~ 2 km, which is in agreement with the range from Dixon (1982) for the depth to the Precambrian-Cambrian contact (between 1.5 and 3 km). The regional model shows that the quartzites are thickened by 6 km, on average, near the range on the western edge of the BRVF, and that the Precambrian-Cambrian contact sits at roughly ~ 8 km depth in the area of the local anomalies of the CDF. The shallowest prisms in the model are in the southwestern region of the model where it reaches a depth of ~ 650 m where the highest gravity

values are located (~ 20 mGal). The regional model is not able to reproduce the highest gravity values (> 18 mGal) without increasing the density contrast, but a higher density contrast does not agree with known densities of quartzite. The model suggests that the regional step in the gravity field is related to the approximate eastern limit of the thickening quartzites in the Meade thrust sheet, but the story is likely more complex.

6.3 Local model of the igneous intrusions

Inversion models of the local CDF gravity anomalies (Figure 5d) are constructed using a wide range of potential density contrasts (-100 kg m^{-3} to -900 kg m^{-3}). The minimum value for the *depth-to-top* parameter is 250 m, based on the approximate thickness of the basalt section (McCurry & Welhan, 2012). This lithologic and mechanical contrast is assumed to introduce a mechanical and compositional boundary that would limit the depth to the top of the intrusions (Kavanagh et al., 2006; Wetmore et al., 2009; Richardson et al., 2015). The maximum value for the *depth-to-bottom* parameter is constrained to 2 km. Maximum prism depths deeper than 2 km tend to produce anomalies of longer wavelength than the observed anomaly.

All best-fit models show two compact bodies in the shallow (< 1 km) subsurface that thin toward their margins, giving them a laccolithic geometry (Roman-Berdiel et al., 1995); the 2 laccolith-shaped bodies have thin or absent prisms between them. Best-fit models show more variation in the prisms' depth to the top while the prisms' depth to the bottom are relatively constant. The best-fit models all have a thick prism (*depth-to-top* ~ 250 m, *depth-to-bottom* ~ 1050 m) located adjacent to China Hat dome. Comparisons of modeled values with the observed gravity show low and unbiased model residuals ($\text{RMSE} \leq 1$ mGal). Many prisms < 100 m thick are poorly constrained by the inversions. Model results indicate that at the location of the Hubbard 25-1 borehole, where layers of basalt are identified in the log at depths of 750 m and 1150 m (Figure 6), model prisms are absent or very thin (≤ 100 m).

The preferred model (Figures 8a and 8b) has a density contrast of -600 kg m^{-3} and a total volume of 63 km^3 . This volume is consistent with the range of volumes found from the excess mass calculation. The southern body has an elliptical shape with long axis ~ 9 km and short axis ~ 6 km, an average thickness of 230 m and a volume of 26 km^3 . The northern body also has an elliptical shape with long axis ~ 10 km and short axis ~ 5.5 km, an average thickness of 320 m and a volume of 37 km^3 . Both bodies have an average depth to center of ~ 750 m. For comparison, another best-fit model with a density contrast of -750 kg m^{-3} , yields 2 model bodies with an average depth to center of 920 m, an average prism thickness of 400 m, and a maximum prism thickness of 770 m. This model has a total volume of 55 km^3 , again agreeing with the excess mass calculation.

As in all gravity models, there is parameter compensation in the tradeoff between density contrast and volume. For example, increasing the density contrast can result in thinner prisms on average, and conversely, decreasing the density contrast can result in thicker prisms. We tested and compiled best-fit models by imposing limits on the density contrast to evaluate the tradeoff between volume and density contrast of the model space. Some of these model results did not have low RMSE. Larger density contrast results in a deeper average depth of the body, but all are relatively shallow (average depth ≤ 1 km).

Figure 9 shows the solutions for 17 simulations, each testing 100,000 – 200,000 parameter combinations. This plot illustrates the tradeoff between density contrast and volume (Blakely, 1994). Solutions have density contrasts between -800 and -400 kg m^{-3} and agree with: (i) lithology observed in the Hubbard 25-1 borehole, (ii) dome density determined from China Cap hand samples and Parasnis/Nettleton density analyses (Nettleton, 1939; Parasnis, 1952), and (iii) volume estimates from mass deficit. A range of

reasonable solutions with nearly identical RMSE occur between density contrasts of -600 to -350 kg m^{-3} . These solutions give a range of volume estimates from ~ 60 to $\sim 120 \text{ km}^3$. The minimum volume of the anomalous mass is $\sim 50 \text{ km}^3$ with a maximum density contrast of approximately -800 kg m^{-3} . Conservatively, the range of total intrusion volume is $50 - 120 \text{ km}^3$.

7 Discussion

7.1 Modeling the gravity anomalies as shallow intrusions

The new gravity data, combined with previous surveys, identifies two large negative anomalies. The addition of marine gravity data constrains the western margin of the northern gravity anomaly, which resides largely under the Blackfoot Reservoir. These data suggest that the large negative gravity anomalies within the CDF are due to high-level silicic intrusions rather than due to a sedimentary basin, as inferred by Mabey & Oriel (1970). If the anomalies were produced by sediments, the basin would be thickest toward the center and the anomaly would have low gravity gradient near its center (Gimenez et al., 2009). Instead, the anomalies show short-wavelength variation where they have the largest negative values. These short-wavelength anomalies indicate that the causative body is actually closer to the surface near the centers of the gravity anomalies. We tested the sedimentary basin model and found poor fits (high RMSE) to the observed gravity data, especially in the center regions of the isolated negative gravity anomalies where the amplitude of the anomalies is high. It is particularly difficult to model basin geometries that create a narrow divide between the two isolated depocenters.

Another key observation is from the Hubbard 25-1 exploration log (Polun, 2011). Anhydrites and siltstones in the upper 700 m suggests that the area of the CDF was submerged and gradually infilled by sediments eroded from the adjacent ranges. However, this section is relatively thin ($\sim 400 \text{ m}$) and has a small density contrast indicating that it is unlikely the negative gravity anomalies are related to a sedimentary basin.

There is an absence of clear basin-bounding normal faults on the eastern and western margins of the BRVF, which supports the idea that a sedimentary basin is not the causative body for these gravity anomalies. The west margin of the modeled intrusion coincides with a west dipping fault with the largest vertical offset (50 m) observed in the BRVF (Figures 10a – c). This sense of offset is concurrent with deformation during the emplacement of shallow intrusions (Acocella, 2000; Acocella et al., 2002; Castro et al., 2016). We note that the sense of offset is opposite of that which would be expected if the fault bounded a sedimentary basin. Overall, the map pattern of faults in the BRVF wraps around the two gravity anomalies, especially on the west side of the reservoir and the fault pattern is consistent with deformation associated with a large intrusion. There are plenty of basins in the region, Gem Valley for example, but all are elongate parallel to basin-bounding faults and none of them exhibit this pattern of faulting.

Shallow intrusion of tabular silicic bodies favors laccolith geometries (Alexander, 1998), consistent with the geometries deduced from the gravity models. Based on the gravity model (Figure 8a and b) with density contrast of -600 kg m^{-3} , the N intrusion has volume 37 km^3 and the S intrusion has volume 26 km^3 .

Both gravity anomalies, and by inference the laccoliths, are slightly elongate NW, perpendicular to the NE (approximately 35°) alignment of silicic domes (Figure 5d). This geometry is consistent with the high-level laccolith intrusion model proposed by Vigneresse et al. (1999). In the absence of substantial volume of intrusion, the unperturbed stress state in the region is extensional, with σ_1 vertical and equal to lithostatic pressure in magnitude. A fracture or dike will propagate vertically and perpendicular to the least principle compressive stress, σ_3 . From the vent alignment we infer that σ_3 is oriented approximately 125° . As the intrusion shallows, the magma pressure exceeds the lithostatic

pressure causing a stress rotation, with σ_3 becoming vertical, resulting in horizontal intrusion. σ_2 becomes oriented approximately 125° and σ_1 approximately 35° , allowing the intrusion to grow faster in a NW-SE direction, perpendicular to the trend of the vent alignment.

The two anomalies may indicate silicic intrusions occurred at two different times, as indicated by the differing ages of BRVF silicic domes. The CDF alignment erupted approximately 58 ka and the Sheep Island dome, forming an island on the west side of the reservoir, erupted approximately 1.5 Ma (McCurry & Welhan, 2012). This difference in dome ages is consistent with at least two episodes of intrusion. Observations of recent high-level silicic intrusions and eruptions indicate that activity frequently involves a complex series of events (Shaffer et al., 2010; Jay et al., 2014; Castro et al., 2016; Miller et al., 2017). If the intrusions in the BRVF formed coeval with the effusion of the domes, similar to the high-level intrusion at Cordón Caulle (Castro et al., 2016), then it is likely that the northern intrusion was emplaced, in a separate event, prior to the southern intrusion.

7.2 Emplacement related deformation

The coincidence of the edges of the negative gravity anomaly with dramatic, if relatively small displacement, faults points to important volcanotectonic interaction during intrusion and silicic dome eruptions (Bursik & Sieh, 1989; Bursik et al., 2003). The faults in the BRVF extend from just north of the town of Soda Springs through the Blackfoot Reservoir, only cutting through bedrock at the surface near the southern end of Pelican Ridge (Figure 2a). While Polun (2011) placed the eastern limit of the rift zone at the discontinuous Hole in the Rock-China Hat fault, we believe, based on topographic data available through the Idaho LiDAR Consortium (Figures 10a – c), that the eastern margin of the rift is an unnamed fault located along the western slopes of the Fox Hills extending north to the east of the Blackfoot Reservoir (Figure 2). The maximum E-W width of the faulting in the BRVF, at the latitude of China Hat, is ~ 10.7 km. The faults in the BRVF are primarily NNW to NNE-trending and exhibit both east and west dips.

The western portion of the fault system in the BRVF includes a prominent nested graben trending N to NNW with the most topographically well-defined portion located just west of the rhyolite domes (Figure 10b). The graben is bounded on the west by the east-dipping Government Road Fault, which has a prominent scarp that is as much as 50 m high. The Government Road Fault is flanked on its west in its central portion by two additional east-dipping faults with scarps as large as 15 m (Figures 2 and 10). The eastern side of the graben is defined by the west-dipping Hole in the Rock and China Hat faults, which appear to be separated by a small left step just north of the China Hat dome (Figures 2 and 10). The graben appears to be floored by a loess-covered surface that is composed of the lavas from several basaltic vents including Red Mountain. The surface steps down >100 m from west to east across a series of east and west-dipping faults creating narrow (~ 50 – 150 m) full and half grabens separated by relatively broad (~ 250 – 750 m) horsts. Throughout the broader graben the surface is typically flat or dipping slightly ($<3^\circ$) east, a slope that appears to have been, at least in part, present before the youngest phase of faulting based on profiles outside the graben to the north and south.

Polun (2011) estimated horizontal extension across the graben from fault displacement and dip. These estimates suggest that the portion of the horst and graben system most proximal to the CDF has the largest magnitude of horizontal extension ranging between 75 and 200 m, depending on the fault dips. The total extension is taken to be a minimum because the estimates did not include all of the faults on the eastern extent of the fault system. The estimates based on minimum extension (i.e., fault dip of 70°) indicate increases from single digits to > 50 m over a distance of 4–5 km on either side

of the CDF. Based on these data, it appears that extension in the BRVF is greatest adjacent to the gravity anomalies and silicic domes, consistent with faulting during emplacement and/or draining of the laccolith.

A set of ENE-trending faults are only found directly overlying the intrusions, especially SW of China Hat dome. These faults appear to be unrelated to the normal tectonic setting of the BRVF. Instead, these faults may have formed during uplift and possibly deflation associated with the intrusions, perhaps associated with the extrusion of magma at the nearby domes (Figures 5d). This ENE-trending fault set is far less pronounced than the other faults in the BRVF (Figure 2b). The average throw across faults in this set is 1–2 m with a maximum of ~ 10 m. Most of the faults are north dipping with the exception of one in the northern third of the set and the three southern-most faults.

Acocella & Funiciello (1999) show that roof lifting associated with the emplacement of a laccolith is viable in producing significant uplift over the intrusion as well as faulting at the margins of the intrusion. We suggest that the pattern of diffuse faulting at the surface is associated with the emplacement of the modeled laccolith and draining of the shallow magmatic system in the extrusion of the CDF rhyolite domes. The highly faulted graben on the west end of the CDF has the greatest extension and lies on the margin of the modeled intrusion geometry. This shows a spatial correlation with the margins of the intrusion and the greatest structurally accommodated extension (Spinks et al., 2005). The amount of horizontal extension that is accommodated is at minimum $\sim 75 - 200$ m in the CDF.

Castro et al. (2016) has shown that shallow (20 – 200 m), rapid intrusion of laccoliths can produce large uplift (> 200 m) and deformation at the margins of intrusion. In the BRVF, we observe the highest magnitude of faulting near the CDF and gravity anomalies with waning surface deformation north and south of the gravity anomalies. Our model suggests that a shallow silicic intrusion of order tens of cubic kilometers was emplaced and dramatically uplifted the BRVF and generated ancillary networks of faults similar to the Cordón Caulle (Castro et al., 2016).

In a more regional context, the BRVF is situated in a complex tectonic setting that may influence the locations of these intrusions. The regional gravity anomaly and model are explained by thickening of a dense quartzite by thrust faulting. Such regional density contrasts in the crust are interpreted to influence magma ascent elsewhere (Deng et al., 2017), possibly explained by changes in stress trajectories associated with the differential loads caused by these broad lithologic variations (Connor et al., 2000; Rivalta et al., 2019).

7.3 Implications for volcanic hazards

The multiple vents of varying ages, the two gravity anomalies and the spatial association with the basaltic volcanic field all indicate that the possibility of future intrusions and dome eruptions should be assessed and that the BRVF deserves monitoring (Ewert et al., 2005). Potential for future silicic eruptions in dominantly basaltic volcanic fields changes the way volcanic hazards need to be estimated (Duffield et al., 1980; Bacon et al., 1980; Jónasson, 2007; Riggs et al., 2019; Kósik et al., 2020). In the BRVF, late Pleistocene silicic domes provide dramatic evidence of silicic eruptions, with an episode forming what is now Sheep Island approximately 1.5 Ma, and an episode forming domes and tuff rings in the CDF approximately 0.06 Ma. The CDF events preserve evidence of explosive volcanism, but are comparable or smaller in volume than nearby and more abundant basaltic eruptions. The interpretation of two gravity anomalies as being caused by large-volume and shallow silicic intrusions changes the hazard, since it indicates these eruptive episodes could have evolved into much larger magnitude and intense eruptions with widespread effects. Even as intrusions, deformation appears to be associated with

the emplacement of these shallow bodies, and is of much larger amplitude than identified in most basaltic volcanic fields.

These intrusions and their associated silicic eruptive vents are widespread. Other examples include large-volume exogeneous and endogeneous silicic domes erupted on the Eastern Snake River Plain, the Buckskin Dome and Ferry Butte south of the town of Blackfoot and Yandell Mountain southeast of Blackfoot (Figure 1). The CDF domes and tuff rings are small-volume compared to these features (0.46 km^3), but the approximately 63 km^3 of the BRVF intrusions is large compared to these other features. From our preferred model the intrusive to extrusive ratio for silicic volcanism is 136:1, but recognizing the range of reasonable volumes from the tradeoff curve (Figure 9) gives an intrusive to extrusive ratio can be between 109:1 and 261:1. While the modeled intrusions are high-volume compared with the mapped eruptive products, we note they are less than one-tenth the volume of the largest caldera eruptions and their intrusive magmas (Gregg et al., 2012; Takarada & Hoshizumi, 2020). Hazards associated with distributed volcanism in this part of the western U.S. and in comparable regions requires silicic volcanism to be included and assessed, in addition to basaltic volcanic hazards.

8 Conclusions

1. A new gravity survey of the BRVF reveals two negative gravity anomalies underlying and adjacent to late Pleistocene silicic domes and tuff rings. These anomalies, after detrending, have amplitudes up to -16 mgal and ellipsoidal shape, elongated NW.
2. The anomalies are modeled as two shallow silicic intrusions, with depth to a nearly flat bottom of 1 km and thickness increasing toward their centers. They are inferred to be silicic laccoliths based on their shapes and the compositions of nearby domes and tuff rings. Given the uncertainty in density of the intrusions, their combined volume is estimated to be in the range of $\sim 50 - 120 \text{ km}^3$. Calculated using density contrast of -600 kg m^{-3} , the northern intrusion has volume 37 km^3 and the southern intrusion has volume 26 km^3 .
3. Significant deformation appears to have accompanied the emplacement of these intrusions. NNW-trending fault sets bound the intrusions, with the largest displacement (50 m) observed on any faults in the BRVF immediately adjacent to the southern intrusion. The gravity anomalies are overlain by ENE-trending faults, which may have formed during emplacement and possibly deflation. It is possible that the ascending magma exploited faults in the BRVF and their ascent was influenced by crustal scale structures associated with thrust faults.
4. At least one and likely two episodes of large-volume and shallow laccolith formation has occurred in the bimodal BRVF. Had these magmas not stalled in the shallowest crust, they would have produced very large magnitude (e.g., VEI 5 or larger) eruptions that would have affected broad areas. We suggest identification and quantification of shallow intrusions may help better quantify volcanic hazards in bimodal volcanic fields. Given the tradeoff between density contrast and volume, the intrusive to extrusive volume ratio for silicic volcanism can range between 109:1 and 261:1.

Acknowledgements

Troy Berkey, Brad Mack, and Tonian Robinson participated in the collection of gravity data in this project. Nigel Brady (Dynamic Gravity Systems) assisted in the collection and processing of marine gravity data. Mathieu Vallee assisted with the logistics of the the marine gravity survey. We are grateful to the Torgansen family for providing access to their land, as well as other landowners in the region for enabling our survey.

This project was supported by a grant from NASA (NNH 16-ESI16-0030). Datasets for this research are available at Hastings et al. (2021).

References

- Acocella, V. (2000). Space accommodation by roof lifting during pluton emplacement at Amiata (Italy). *Terra Nova*, 12(4), 149–155.
- Acocella, V., & Funicello, R. (1999). The interaction between regional and local tectonics during resurgent doming: the case of the island of Ischia, Italy. *Journal of Volcanology and Geothermal Research*, 88(1-2), 109–123.
- Acocella, V., Pascucci, V., & Dominici, G. (2002). Basin deformation due to laccolith emplacement at Radicofani (Southern Tuscany, Italy). *Boll. Soc. Geol. It., Volume Speciale*, 1, 749–756.
- Agustsdottir, T., Gudmundsson, M. T., & Einarsson, P. (2011). A gravity study of silicic domes in the Krafla area, N-Iceland. *Jokull*, 60, 135–148.
- Alexander, R. C. (1998). On the emplacement of tabular granites. *Journal of the Geological Society*, 155(5), 853–862.
- Anders, M. H., Geissman, J., Piety, L. A., & Sullivan, J. (1989). Parabolic distribution of circumeastern Snake River Plain seismicity and Latest Quaternary faulting: Migratory pattern and association with the Yellowstone Hotspot. *Journal of Geophysical Research: Solid Earth*, 94(82), 1589–1621.
- Armstrong, F. C., & Oriel, S. S. (1965). Tectonic development of Idaho-Wyoming thrust belt. *AAPG Bulletin*, 49(11), 1847–1866.
- Avellán, D. R., Macías, J. L., Pardo, N., Scolamacchia, T., & Rodriguez, D. (2012). Stratigraphy, geomorphology, geochemistry and hazard implications of the Nejapa Volcanic Field, western Managua, Nicaragua. *Journal of Volcanology and Geothermal Research*, 213, 51–71.
- Bacon, C. R. (1982). Time-predictable bimodal volcanism in the Coso Range, California. *Geology*, 10(2), 65–69.
- Bacon, C. R., Duffield, W. A., & Nakamura, K. (1980). Distribution of Quaternary rhyolite domes of the Coso Range, California: Implications for extent of the geothermal anomaly. *Journal of Geophysical Research: Solid Earth*, 85(B5), 2425–2433.
- Battaglia, M., Segall, P., & Roberts, C. (2003). The mechanics of unrest at Long Valley caldera, California. 2. Constraining the nature of the source using geodetic and micro-gravity data. *Journal of Volcanology and Geothermal Research*, 127(3-4), 219–245.
- Blakely, R. J. (1994). Extent of partial melting beneath the Cascade Range, Oregon: Constraints from gravity anomalies and ideal-body theory. *Journal of Geophysical Research: Solid Earth*, 99(B2), 2757–2773.
- Blakely, R. J. (1996). *Potential Theory in Gravity and Magnetic Applications*. Cambridge University Press.
- Bott, M. H. P., & Smithson, S. B. (1967). Gravity investigations of subsurface shape and mass distributions of granite batholiths. *Geological Society of America, Bulletin*, 78(7), 859–878.
- Bursik, M., Renshaw, C., McCalpin, J., & Berry, M. (2003). A volcanotectonic cascade: Activation of range front faulting and eruptions by dike intrusion, Mono Basin-Long Valley Caldera, California. *Journal of Geophysical Research: Solid Earth*, 108(B8).
- Bursik, M., & Sieh, K. (1989). Range front faulting and volcanism in the Mono Basin, eastern California. *Journal of Geophysical Research: Solid Earth*, 94(B11), 15587–15609.
- Castro, J. M., Cordonnier, B., Schipper, C. I., Baumann, H. T. T. S., & Feisel, Y. (2016). Rapid laccolith intrusion driven by explosive volcanic eruption. *Nature*

- 606 *Communications*, 7(1), 1–7.
- 607 Connor, C. B., Sparks, R., Díez, M., Volentik, A., & Pearson, S. (2009). The na-
 608 ture of volcanism. In C. B. Connor, N. Chapman, & L. Connor (Eds.), *Volcanic*
 609 *and Tectonic Hazard Assessment for Nuclear Facilities* (pp. 74–115). Cambridge,
 610 England: Cambridge University Press.
- 611 Connor, C. B., Stamatakis, J. A., Ferrill, D. A., Hill, B. E., Ofoegbu, G. I., Conway,
 612 F. M., ... Trapp, J. (2000). Geologic factors controlling patterns of small-volume
 613 basaltic volcanism: Application to a volcanic hazards assessment at Yucca Moun-
 614 tain, Nevada. *Journal of Geophysical Research: Solid Earth*, 105(B1), 417–432.
- 615 Deng, F., Connor, C. B., Malservisi, R., Connor, L. J., White, J. T., Germa, A., &
 616 Wetmore, P. H. (2017). A geophysical model for the origin of volcano vent clus-
 617 ters in a Colorado Plateau volcanic field. *Journal of Geophysical Research: Solid*
 618 *Earth*, 122(11), 8910–8924.
- 619 Dixon, J. S. (1982). Regional structural synthesis, Wyoming Salient of Western
 620 Overthrust Belt. *AAPG Bulletin*, 66(10), 1560–1580.
- 621 Duffield, W. A., Bacon, C. R., & Dalrymple, G. B. (1980). Late Cenozoic volcanism,
 622 geochronology, and structure of the Coso range, Inyo County, California. *Journal*
 623 *of Geophysical Research: Solid Earth*, 85(B5), 2381–2404.
- 624 Ewert, J. W., Guffanti, M., & Murray, T. L. (2005). *An assessment of volcanic*
 625 *threat and monitoring capabilities in the United States: framework for a National*
 626 *Volcano Early Warning System* (Tech. Rep.). Reston, VA: US Geological Survey.
- 627 Ferrill, D. A., Stamatakis, J. A., & Sims, D. (1999). Normal fault corrugation: Im-
 628 plications for growth and seismicity of active normal faults. *Journal of Structural*
 629 *Geology*, 21(8-9), 1027–1038.
- 630 Finn, C., & Williams, D. L. (1982). Gravity evidence for a shallow intrusion under
 631 Medicine Lake volcano, California. *Geology*, 10(10), 503–507.
- 632 Garibaldi, N., Tikoff, B., Peterson, D., Davis, J. R., & Keranen, K. (2020). Sta-
 633 tistical separation of tectonic and inflation-driven components of deformation on
 634 silicic reservoirs, Laguna del Maule volcanic field, Chile. *Journal of Volcanology*
 635 *and Geothermal Research*, 389, 106744.
- 636 George, O. A., Malservisi, R., Govers, R., Connor, C. B., & Connor, L. J. (2016).
 637 Is uplift of volcano clusters in the Tohoku Volcanic Arc, Japan, driven by magma
 638 accumulation in hot zones? A geodynamic modeling study. *Journal of Geophysical*
 639 *Research: Solid Earth*, 121(6), 4780–4796.
- 640 Gimenez, M. E., Martinez, M. P., Jordan, T., Ruiz, F., & Klinger, F. L. (2009).
 641 Gravity characterization of the La Rioja Valley basin, Argentina. *Geophysics*,
 642 74(3), B83–B84.
- 643 Glocker, M., Landau, H., Leandro, R., & Nitschke, M. (2012). Global precise multi-
 644 GNSS positioning with Trimble Centerpoint RTX. In *2012 6th ESA Workshop on*
 645 *Satellite Navigation Technologies (Navitec 2012) & European Workshop on GNSS*
 646 *Signals and Signal Processing* (pp. 1–8).
- 647 Gómez-Vasconcelos, M. G., J. L. Macías, D. R. A., Sosa-Ceballos, G., Garduño-
 648 Monroy, V. H., Cisneros-Máximo, G., Layer, P. W., ... others (2020). The control
 649 of preexisting faults on the distribution, morphology, and volume of monogenetic
 650 volcanism in the Michoacán-Guanajuato Volcanic Field. *Geological Society of*
 651 *America Bulletin*, 30, 2455–2474.
- 652 Gottsmann, J., Lavallée, Y., Martí, J., & Aguirre-Díaz, G. (2009). Magma–tectonic
 653 interaction and the eruption of silicic batholiths. *Earth and Planetary Science Let-*
 654 *ters*, 284(3-4), 426–434.
- 655 Gregg, P. M., DeSilva, S. L., Grosfils, E. B., & Parmigiani, J. P. (2012). Catastrophic
 656 caldera-forming eruptions: Thermomechanics and implications for eruption
 657 triggering and maximum caldera dimensions on Earth. *Journal of Volcanology and*
 658 *Geothermal Research*, 241, 1–12.
- 659 Hastings, M. S., Connor, C. B., Malservisi, R., Rodgers, M., & Connor, L. J. (2021).

- Blackfoot reservoir volcanic field gravity data. <https://zenodo.org/record/4749647#.YLTWnnVKhhE>. doi: 10.5281/zenodo.4749647
- Heumann, A. (2004). Timescales of evolved magma generation at Blackfoot Lava Field. In *Volcanism and Its Impacts on Society*. International Association of Volcanology and Chemistry of the Earth's Interior (IAVCEI).
- Hinze, W. J. (2003). Bouguer reduction density, why 2.67? *Geophysics*, 68(5), 1559–1560.
- Jay, J., Costa, F., Pritchard, M., Lara, L., Singer, B., & Herrin, J. (2014). Locating magma reservoirs using InSAR and petrology before and during the 2011–2012 Cordón Caulle silicic eruption. *Earth and Planetary Science Letters*, 395, 254–266.
- Jónasson, K. (2007). Silicic volcanism in Iceland: Composition and distribution within the active volcanic zones. *Journal of Geodynamics*, 43(1), 101–117.
- Kavanagh, J. L., Menand, T., & Sparks, R. S. J. (2006). An experimental investigation of sill formation and propagation in layered elastic media. *Earth and Planetary Science Letters*, 245(3–4), 799–813.
- Keller, G. R., Hildenbrand, T. G., Kucks, R., Webring, M., Briesacher, A., Rujawitz, K., ... others (2006). A community effort to construct a gravity database for the United States and an associated Web portal. *Special Papers – Geological Society of America*, 397, 21.
- Kósik, S., Bebbington, M., & Németh, K. (2020). Spatio-temporal hazard estimation in the central silicic part of Taupo Volcanic Zone, New Zealand, based on small to medium volume eruptions. *Bulletin of Volcanology*, 82, 1–15.
- Lowenstern, J. B., Clynne, M. A., & Bullen, T. D. (1997). Comagmatic A-type granophyre and rhyolite from the Alid volcanic center, Eritrea, northeast Africa. *Journal of Petrology*, 38(12), 1707–1721.
- Mabey, D. R., & Oriel, S. S. (1970). *Gravity and magnetic anomalies in the Soda Springs region, southeastern Idaho* (Tech. Rep.). Reston, VA: US Government Printing Office.
- Mastin, L. G., & Pollard, D. D. (1988). Surface deformation and shallow dike intrusion processes at Inyo Craters, Long Valley, California. *Journal of Geophysical Research: Solid Earth*, 93(B11), 13221–13235.
- Mazzarini, F., Corti, G., Manetti, P., & Innocenti, F. (2004). Strain rate and bimodal volcanism in the continental rift: Debre Zeyt volcanic field, northern MER, Ethiopia. *Journal of African Earth Sciences*, 39(3–5), 415–420.
- McCurry, M., & Welhan, J. (2012). Do magmatic-related geothermal energy resources exist in southeast Idaho. *Geothermal Research Council, Transactions*, 36, 699–707.
- McCurry, M., Welhan, J., Polun, S., Autenrieth, K., & Rodgers, D. W. (2011). Geothermal potential of the Blackfoot Reservoir-Soda Springs volcanic field: A hidden geothermal resource and natural laboratory in SE Idaho. *Geothermal Research Council, Transactions*, 35, 917–924.
- Miller, C. A., Williams-Jones, G., Fournier, D., & Witter, J. (2017). 3D gravity inversion and thermodynamic modelling reveal properties of shallow silicic magma reservoir beneath Laguna del Maule, Chile. *Earth and Planetary Science Letters*, 459, 14–27.
- Nelder, J. A., & Mead, R. (1965). A simplex method for function minimization. *The Computer Journal*, 7(4), 308–313.
- Nettleton, L. L. (1939). Determination of density for reduction of gravimeter observations. *Geophysics*, 4(3), 176–183.
- Oriel, S. S., & Platt, L. B. (1980). *Geologic Map of Preston 1 x 2 (degree) quadrangle southeastern Idaho and western Wyoming*. U.S. Geological Survey.
- Parasnis, D. S. (1952). A study of rock densities in the English Midlands. *Geophysical Supplements to the Monthly Notices of the Royal Astronomical Society*, 6(5),

- 252–271.
- Pardo, N., Macias, J. L., Giordano, G., Cianfarra, P., Avellán, D. R., & Bellatreccia, F. (2009). The ~1245 yr BP Asososca maar eruption: The youngest event along the Nejapa–Miraflores volcanic fault, Western Managua, Nicaragua. *Journal of Volcanology and Geothermal Research*, 184(3–4), 292–312.
- Parker, R. L. (1974). Best bounds on density and depth from gravity data. *Geophysics*, 39(5), 644–649.
- Paulatto, M., Moorkamp, M., Hautmann, S., Hooft, E., Morgan, J. V., & Sparks, R. S. J. (2019). Vertically extensive magma reservoir revealed from joint inversion and quantitative interpretation of seismic and gravity data. *Journal of Geophysical Research: Solid Earth*, 124(11), 11170–11191.
- Polun, S. (2011). *Kinematic Analysis of Late Pleistocene Faulting in the Blackfoot Lava Field, Caribou County, Idaho* (Unpublished master’s thesis). Idaho State University.
- Press, W. H., Teukolsky, S. A., Vetterling, W. T., & Flannery, B. P. (2007). *Numerical Recipes 3rd edition: The Art of Scientific Computing*. Cambridge University Press.
- Richardson, J., Connor, C., Wetmore, P. H., Connor, L., & Gallant, E. (2015). Role of sills in the development of volcanic fields: Insights from lidar mapping surveys of the San Rafael Swell, Utah. *Geology*, 43(11), 1023–1026.
- Riggs, N., Ort, M., Connor, C., Alfano, F., & Conway, M. (2019). Volcanology and associated hazards of the San Francisco volcanic field. *Geological Excursions in Southwestern North America*, 55, 127–146.
- Rivalta, E., Corbi, F., Passarelli, L., Acocella, V., Davis, T., & Di Vito, M. A. (2019). Stress inversions to forecast magma pathways and eruptive vent location. *Science Advances*, 5(7), eaau9784.
- Roman-Berdiel, T., Gapais, D., & Brun, J. (1995). Analogue models of laccolith formation. *Journal of Structural Geology*, 17(9), 1337–1346.
- Saballos, J. A., Malservisi, R., Connor, C. B., LaFemina, P., & Wetmore, P. (2013). Gravity and geodesy of Concepción volcano, Nicaragua. *Geological Society of America Special Papers*, 498, 77–88.
- Shaffer, W., Bursik, M., & Renshaw, C. (2010). Elastic source model of the North Mono eruption (1325–1368 AD) based on shoreline deformation. *Bulletin of Volcanology*, 72(10), 1141–1152.
- Sparks, R. S. J. (2003). Forecasting volcanic eruptions. *Earth and Planetary Science Letters*, 210(1–2), 1–15.
- Spinks, K. D., Acocella, V., Cole, J. W., & Bassett, K. N. (2005). Structural control of volcanism and caldera development in the transtensional Taupo Volcanic Zone, New Zealand. *Journal of Volcanology and Geothermal Research*, 144(1–4), 7–22.
- Suneson, N. H. a. I. L. (1983). Origin of bimodal volcanism, southern Basin and Range province, west-central Arizona. *Geological Society of America Bulletin*, 94(8), 1005–1019.
- Takarada, S., & Hoshizumi, H. (2020). Distribution and eruptive volume of Aso-4 pyroclastic density current and tephra fall deposits, Japan: a M8 super-eruption. *Frontiers in Earth Science*, 8, 170.
- Tanaka, K. L., Shoemaker, E. M., Ulrich, G. E., & Wolfe, E. W. (1986). Migration of volcanism in the San Francisco volcanic field, Arizona. *Geological Society of America Bulletin*, 97(2), 129–141.
- Telford, W. M., Geldart, L. P., & Sheriff, R. E. (1990). *Applied geophysics*. Cambridge University Press.
- Tuffen, H., & Dingwell, D. (2005). Fault textures in volcanic conduits: evidence for seismic trigger mechanisms during silicic eruptions. *Bulletin of Volcanology*, 67(4), 370–387.
- Vignerresse, J.-L., Tikoff, B., & Améglio, L. (1999). Modification of the re-

- 768 gional stress field by magma intrusion and formation of tabular granitic plutons.
 769 *Tectonophysics*, 302(3-4), 203–224.
- 770 Wetmore, P. H., Connor, C. B., Kruse, S. E., Callihan, S., Pignotta, G., Stremtan,
 771 C., & Burke, A. (2009). Geometry of the Trachyte Mesa intrusion, Henry Moun-
 772 tains, Utah: Implications for the emplacement of small melt volumes into the
 773 upper crust. *Geochemistry, Geophysics, Geosystems*, 10(8).
- 774 White, J. T., Karakhanian, A., Connor, C. B., Connor, L. J., Hughes, J. D.,
 775 Malservisi, R., & Wetmore, P. (2015). Coupling geophysical investigation with
 776 hydrothermal modeling to constrain the enthalpy classification of a potential
 777 geothermal resource. *Journal of Volcanology and Geothermal Research*, 298,
 778 59–70.
- 779 Wood, M. S., Skinner, K. D., & Fosness, R. L. (2011). *Bathymetry and capacity*
 780 *of Blackfoot Reservoir, Caribou County, Idaho, 2011* (No. 3229). U.S. Geological
 781 Survey.

782

9 Figures

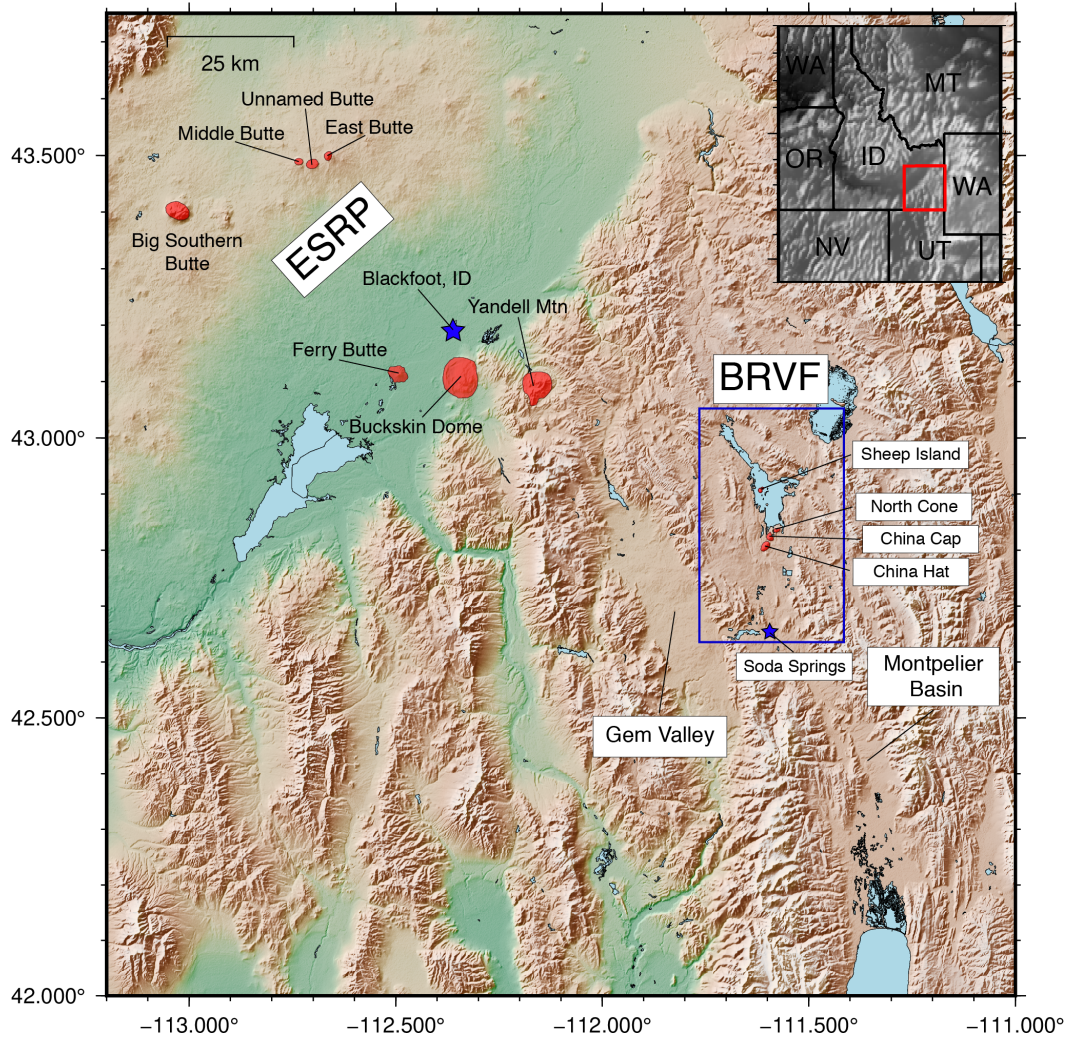


Figure 1. The Blackfoot Reservoir volcanic field (BRVF) is situated roughly 50 – 60 km south-east of the Eastern Snake River Plain (ESRP), adjacent to Gem Valley and Montpelier Basin. The BRVF (blue box) is approximately 50 × 25 km and includes the town of Soda Springs, ID (blue star), and the Blackfoot Reservoir (light blue, SE–NW-trending water body inside darker blue box). All bodies of water are light blue; rhyolitic domes are bright red. The source for the DEM is 3 arc second SRTM data (reference ?).

783

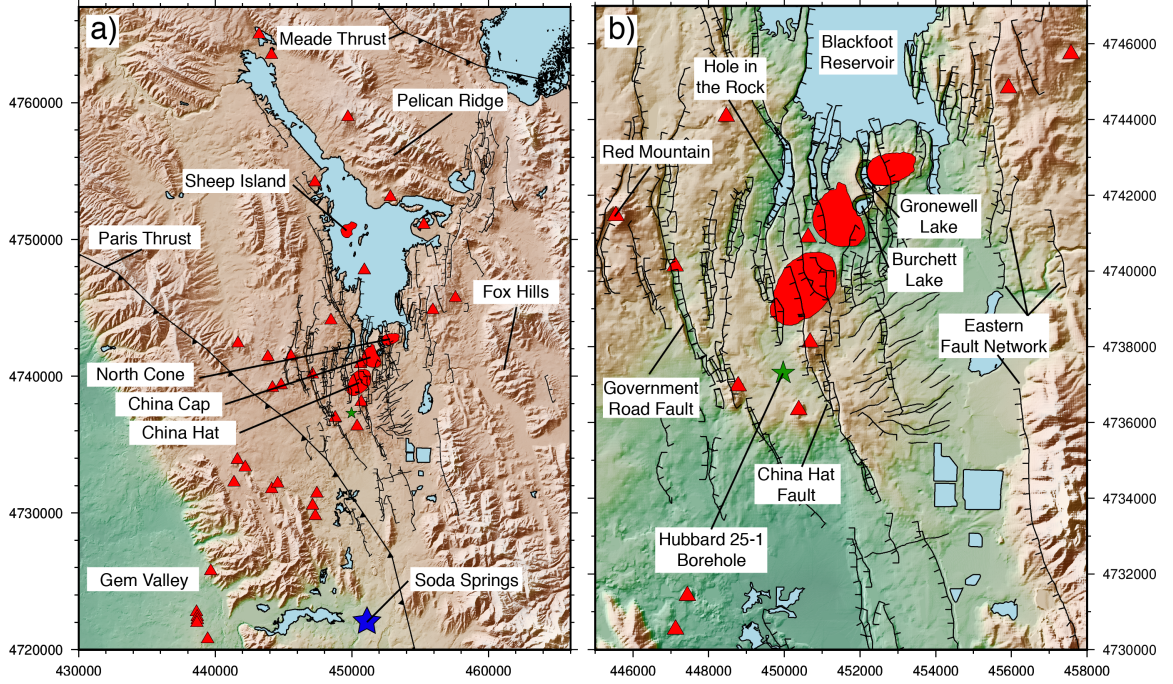


Figure 2. The a) BRVF and b) Central Dome Field (CDF) lie within UTM Zone 12T. The CDF comprises the three rhyolitic domes on the south end of the Blackfoot Reservoir (China Hat, China Cap, and North Cone). The E–W extent of faulting in the BRVF is defined by Government Road Fault to the west and the Eastern Fault Network, labeled on (b). Faults are represented by black lines with throw markers indicating the sense of offset on N–NNW trending faults. ENE trending faults, southeast of the China Hat dome, do not have throw markers because their offset is subdued compared to the N–NNW faults. The Burchett Lake and Gronewell Lake tuff rings location between the China Cap and North Cone domes (bright red patches) provide evidence of previous phreatomagmatic eruptions within the BRVF. The Meade and Paris thrust faults define the approximate edge of the Idaho-Wyoming Thrust Belt remnant from the Sevier Orogeny (Armstrong & Oriol, 1965). The Hubbard 25-1 borehole is represented by the green star and an interpreted lithology log and density profile of the borehole can be seen in Figure 6. Red triangles show basaltic vents.

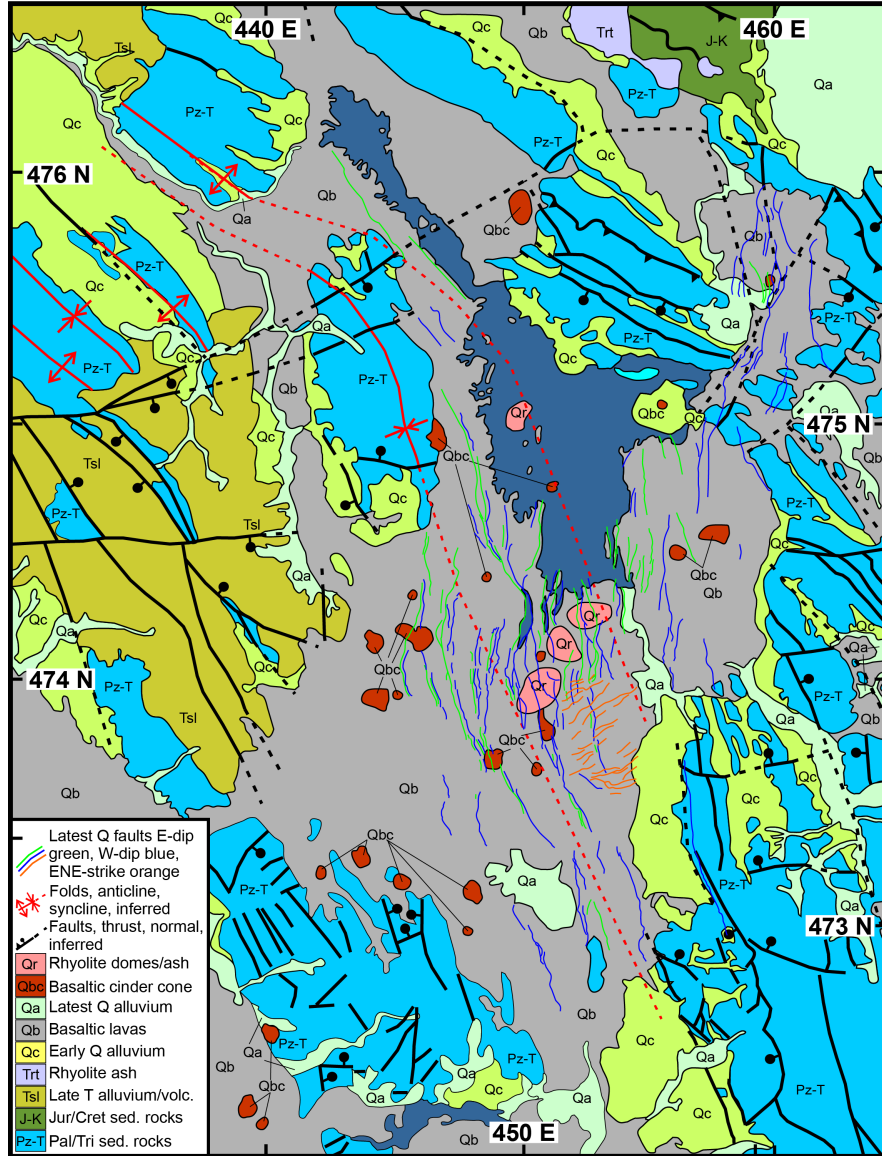


Figure 3. Geologic map of the BRVF, modified from Oriel & Platt (1980), shows that the Quaternary basalts cover the valley floor and flowed towards the town of Soda Springs to the south and Gem Valley to the southwest. The faults in the BRVF show a distinctly different trend/orientation relative to the bedrock faults in the adjacent ranges.

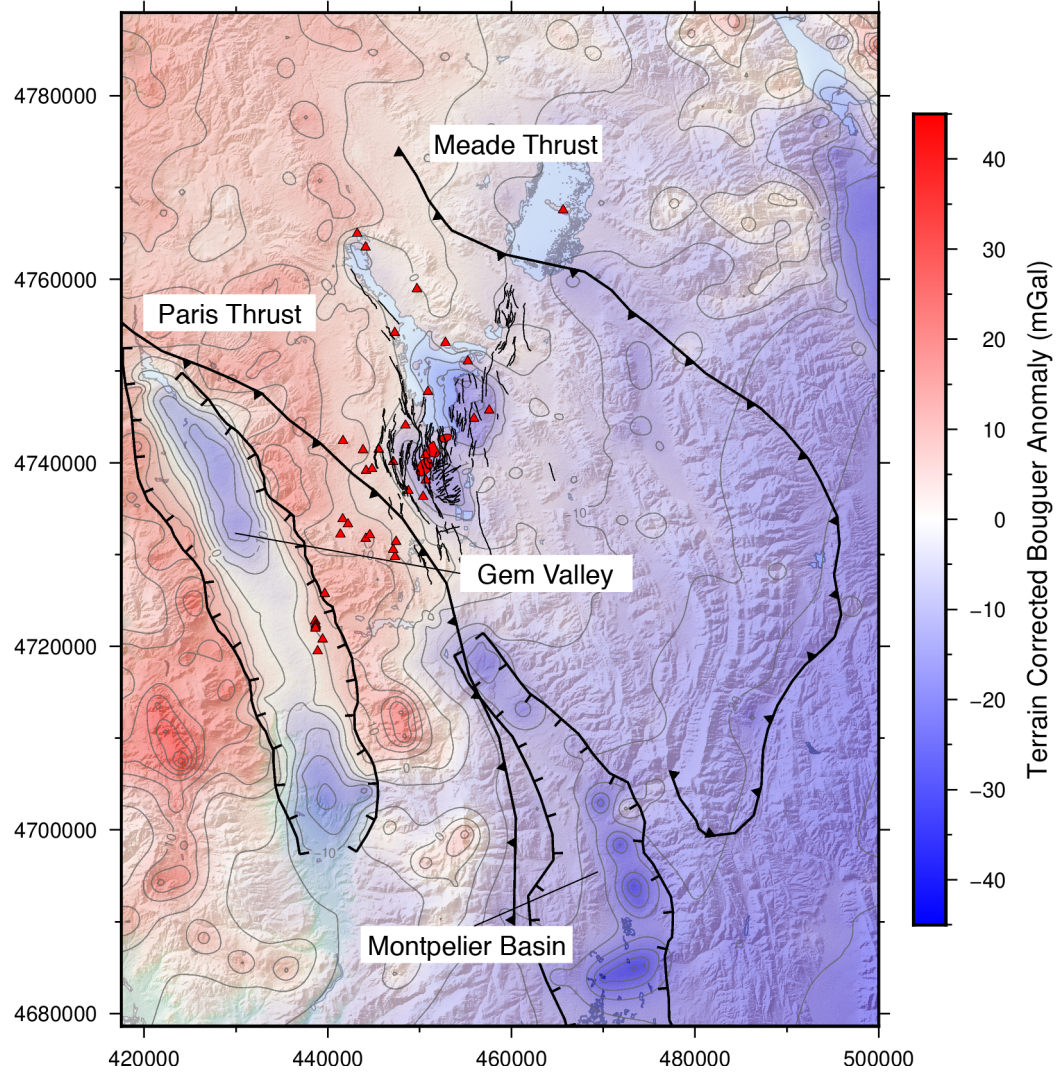


Figure 4. Terrain-corrected Bouguer gravity anomaly from the region surrounding the BRVF, SE Idaho. This map is contoured using older USGS data and our new terrestrial and marine gravity data. The more negative basin anomalies of Gem Valley (west of the BRVF) and Montpelier Basin (south of the BRVF) are evident.

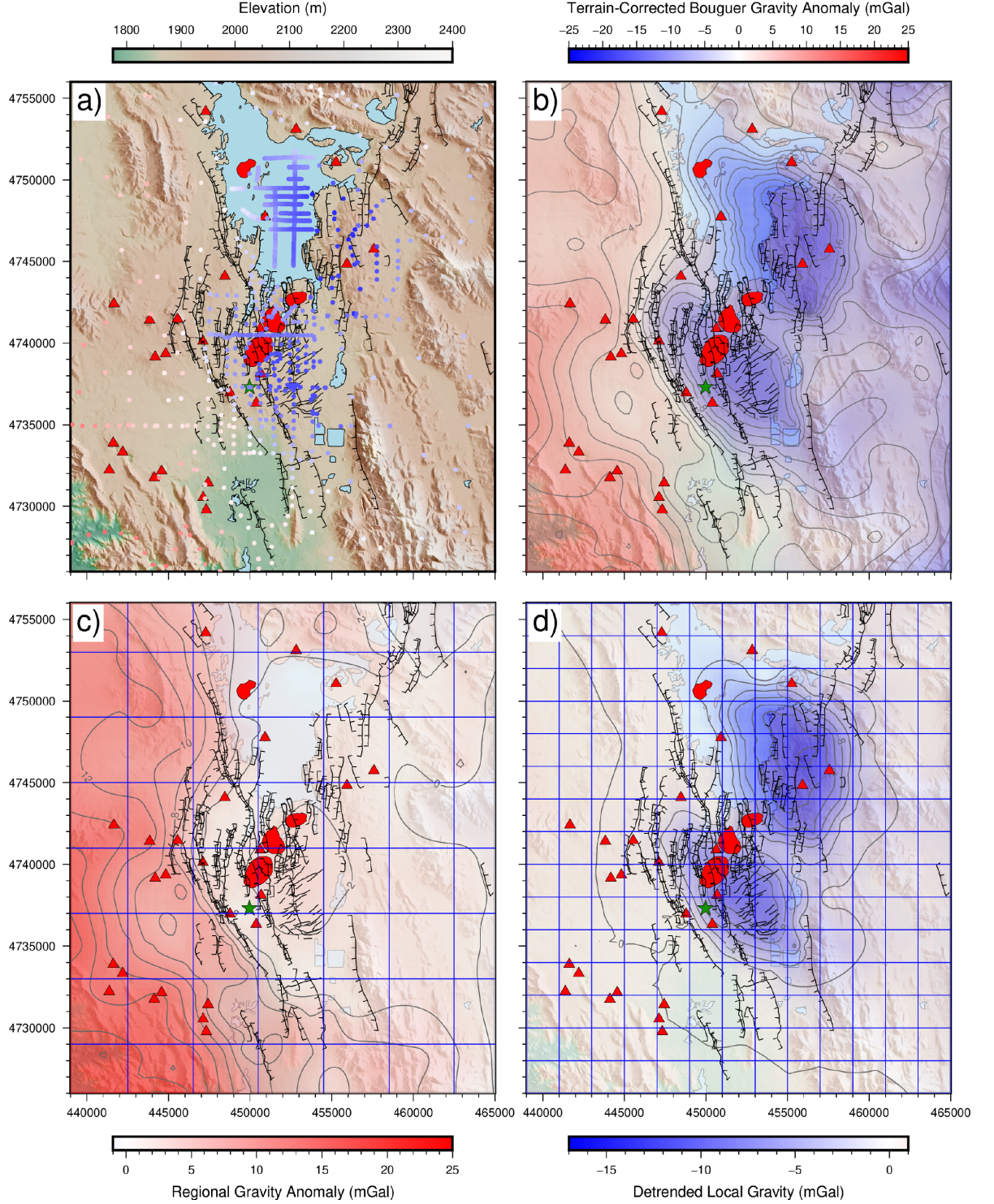


Figure 5. Gravity maps overlain on a 10 m hillshade DEM (USGS), with faults, domes, and vents. Normal faults are marked by black lines with throw markers; ENE trending faults south-east of the rhyolitic domes (red patches) are black lines without throw markers. Basaltic vents are red triangles. The Hubbard 25-1 borehole (green star, Figure 6) is located just south of China Hat dome. The map region is constrained to the data bounds used for the inversions. (a) locations of gravity data colored by terrain-corrected Bouguer anomaly value, b) terrain-corrected Bouguer gravity, c) regional and d) local gravity anomalies. Blue grid lines show the prisms boundaries used in the respective inversions. Prisms for the regional model (c) are 4×4 km and extend slightly past the data bounds to minimize edge effects; prisms for the local model (d) are 2×2 km.

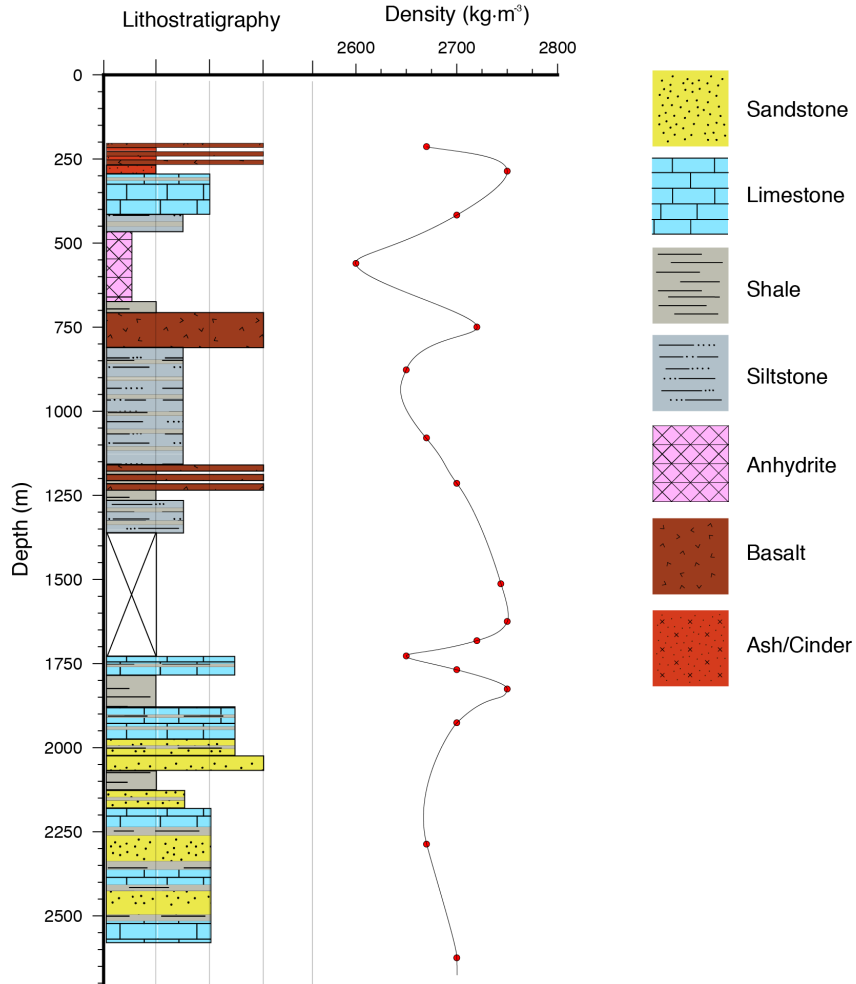


Figure 6. Lithology and density profiles are interpreted from the Hubbard 25-1 borehole data, located about 1 km S of China Hat dome, on the hanging wall W of the normal fault with large throw (about 50 m) and bounds the modeled intrusion (green star in Figure 2). The average host rock density through the upper 2.5 km in the BRVF is 2700 kg m^{-3} , and adds to the density contrast causing the negative CDF gravity anomalies.

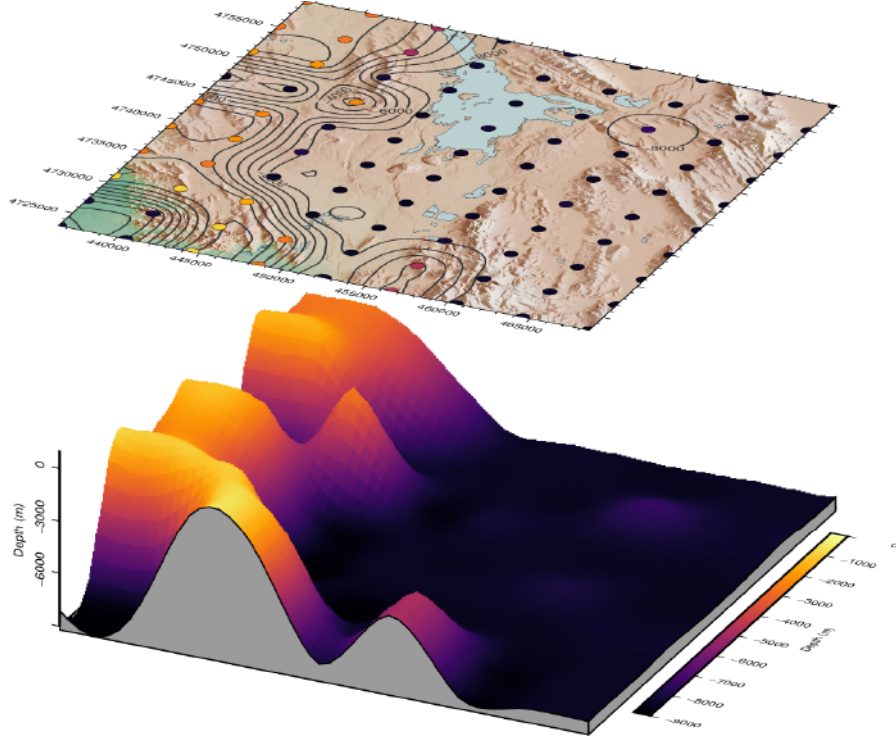


Figure 7. The top perspective image depicts the CDF over the extent of the prisms for the inversion of the regional anomaly. The centers of the prisms are represented by circles that are colored and contoured by the depth to the tops of the prisms. The bottom depth of this model is uniform at 8.1 km and the model density contrast is 150 kg m^{-3} . The bottom plot is a 3D perspective mesh of the tops of the prisms and is colored by depth-to-top. This model shows that a thickening of high density quartzites is a possible cause of the regional anomaly.

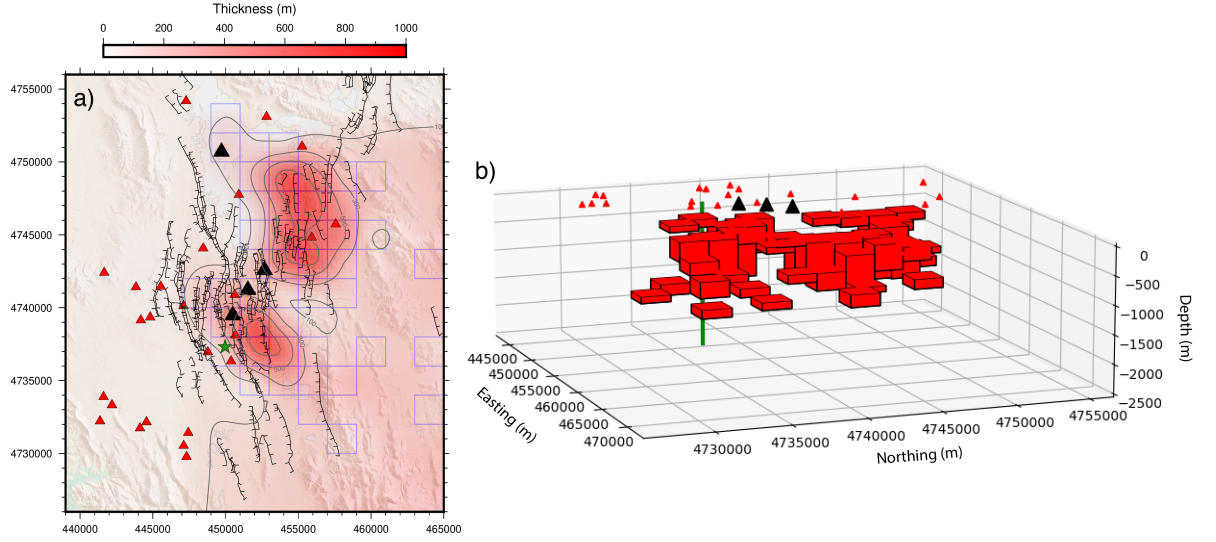


Figure 8. Inversion of the gravity data creates a subsurface geometry consistent with silicic intrusions. The modeled density contrast is -600 kg m^{-3} ; the deepest prism extends to a depth of 1.2 km. Thickness contours of the modeled prism geometry (a) are plotted over a 10-m hill-shade DEM with faults, vents, and domes superimposed. Model prisms with thickness $>100 \text{ m}$, are outlined with blue squares that underlay the thickness contours. A 3D perspective of the prism geometry with 5 times vertical exaggeration (b) illustrates the separation between the two distinct bodies modeled by the inversion. Basaltic vents and rhyolitic domes are represented by red and black triangles respectively; faults are marked by black lines with fault throws; location of the Hubbard 25-1 borehole, detailed in Figure 6, is depicted by a green star (a) and green cylinder (b).

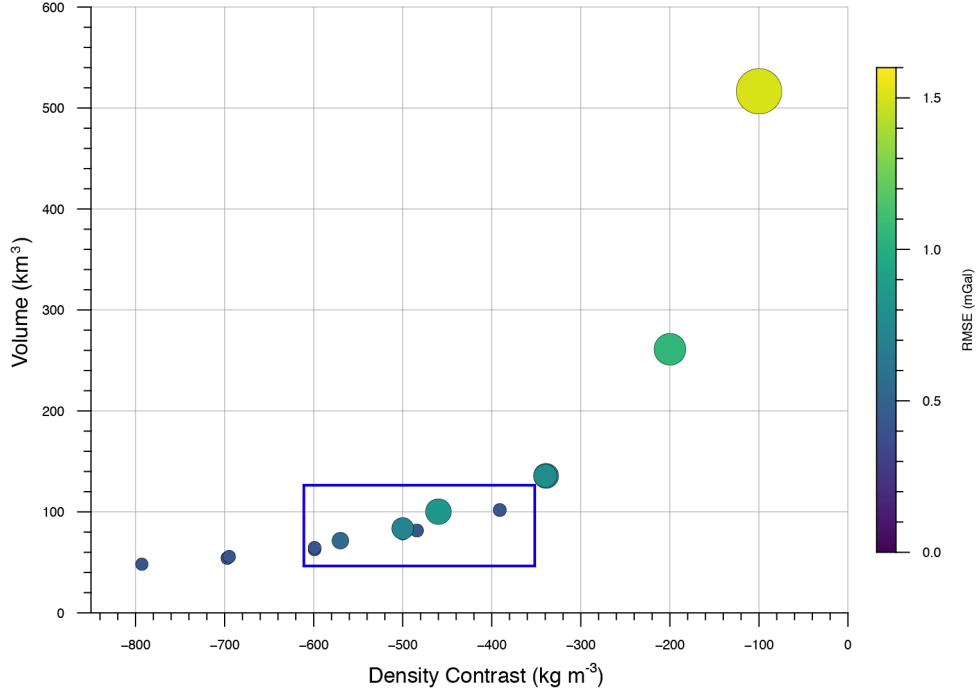


Figure 9. The trade-off between density contrast and volume is illustrated using 17 different inversions. Each circle represents an inversion result; the size/color of the circle corresponds to the goodness-of-fit (RMSE) of the inversion. Inversion results give a minimum intrusion volume of $\sim 50 \text{ km}^3$ with a maximum density contrast of approximately -800 kg m^{-3} . A range of reasonable solutions between -600 and -350 kg m^{-3} that have respective volumes between ~ 60 and $\sim 120 \text{ km}^3$ is identified by the blue box.

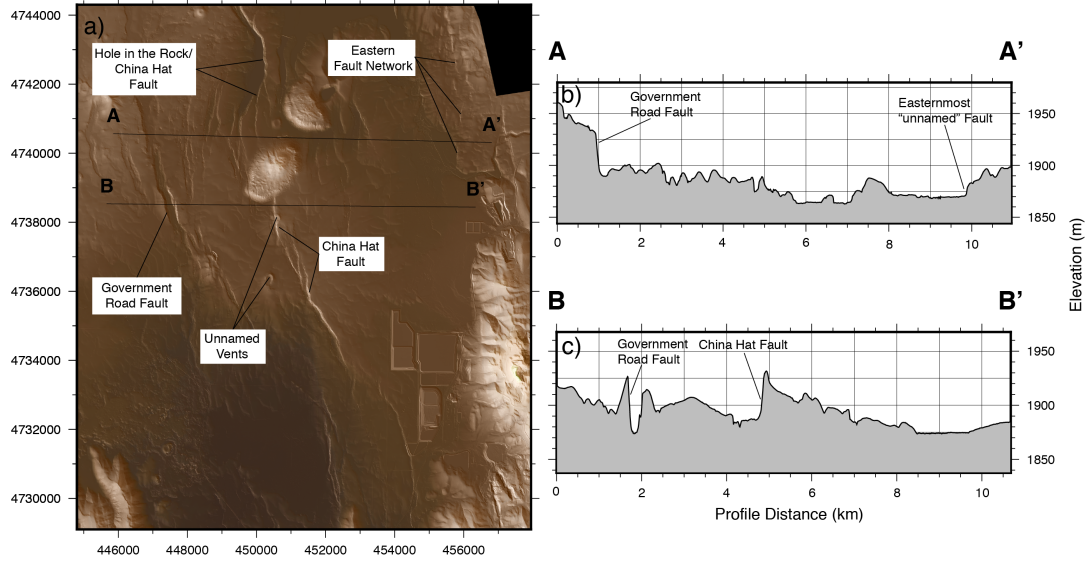


Figure 10. A 1-m LiDAR hillshade of the CDF, illuminated from the SW (a), reveals fault scarps on the western side of the CDF. Profile AA' (b) shows a localized region of faulting from 1 km to 5 km distance. The profile illuminates many horsts and grabens, bumps on the profile line, across this short distance that are absent in the BB' profile. The Eastern Fault Network can be seen clearly in the LiDAR and shows that the faulting continues to the east of the domes. Profile BB' (c) shows that the continuation of the localized faulting from the AA' profile terminates to the south. It also illuminates the magnitude of offset on the China Hat Fault ($\sim 45\text{--}50\text{ m}$) which bounds the western margin of the modeled intrusion (Figure 8). Both profiles have $25\times$ vertical exaggeration.